



Research Article

Daily Variation and Regional Differences in Wind Power Output during Heat and Cold Wave Days in China

Yang Liu ¹ and Jie Bai ²

¹Key Laboratory of Land Surface Pattern and Simulation, Institute of Geographic Sciences and Natural Resources Research, Chinese Academy of Sciences, Beijing 100101, China

²China Electric Power Research Institute Co., Ltd., Beijing 100192, China

Correspondence should be addressed to Jie Bai; baijie@epri.sgcc.com.cn

Received 25 December 2022; Revised 30 June 2023; Accepted 13 July 2023; Published 19 September 2023

Academic Editor: Xueqian Fu

Copyright © 2023 Yang Liu and Jie Bai. This is an open access article distributed under the Creative Commons Attribution License, which permits unrestricted use, distribution, and reproduction in any medium, provided the original work is properly cited.

China currently boasts the largest installed capacity of wind power; however, its output is unstable and highly dependent on weather variability. Despite this, the influence of extreme weather events on wind energy production at the interprovincial scale in China has not been fully characterized. This study aims at investigating the daily variations and regional differences in wind power output during heat wave (HW) and cold wave (CW) days in six regions of China. In addition, the study projects the monthly changes in HW and CW days in the coming decades by utilizing a stacking ensemble machine learning method. The projections are under a real-world warming scenario that incorporates current and long-term actions or policies. The findings of the study reveal that, for most regions, the daily cumulative wind power generation on HW days is close to that on normal days; however, there is a lower output during the daytime and a higher output at night. Furthermore, the number of HW days is projected to increase by 2.3 to 21.8 days during the periods of 2031–2040, 2041–2050, and 2051–2060 in these regions. By comparison, the daily cumulative wind power generation increases significantly on CW days, and the monthly distribution of CW days is expected to undergo notable changes in the future. These findings provide valuable insights into wind resource planning and operation under extreme weather conditions in China.

1. Introduction

China boasts the world's largest installed capacity and second-largest technical resource potential for onshore wind power [1–3]. By the end of 2021, China's installed wind power capacity and electricity generation had reached 328 GW and 655.8 PWh, respectively, accounting for 13.8% and 7.8% of the country's total volumes and playing an irreplaceable role in the country's industrial sectors [4]. At the national level, wind power ranks second among all clean energy resources (nuclear and renewables) after hydropower in China, while wind energy is unevenly distributed at the provincial level. The installed capacity or electricity generation from wind power ranks first among all renewables for 13 provinces, including Hebei, Shanxi, Inner Mongolia, Liaoning, Jilin, Heilongjiang, Ningxia, Xinjiang, Henan,

Gansu, Shanghai, Jiangsu, and Shandong. Although wind power makes an important contribution to the electric system for many provinces in China, the energy output of a wind farm is unstable and highly dependent on weather variability. The wind power output suffers significant fluctuations with the occurrence of different weather conditions, especially regional extreme weather events [5–10].

China proposed to reach peak carbon emissions around 2030 and achieve carbon neutrality before 2060, which requires a substantial growth of renewable energies and collaborative optimizations among various energy resources [11]. Specifically, the onshore wind power installation is anticipated to reach 1866 GW [12, 13]. In addition, the frequency or intensity of extreme weather events in China is projected to increase for the next several decades in the context of global warming [14, 15]. For example, the average

heat wave (HW) days and HW duration in 2020–2039 is projected to be 1.86 (2.53) and 1.56 (2.00) times higher than that in 1986–2015 under the 1.5°C (2.0°C) warming levels. This increase in extreme weather events poses challenges to uncertainty planning in distributed renewable energy systems [16, 17]. Therefore, it is essential to understand the characteristics of wind power output under extreme weather events such as HW and cold wave (CW).

Some case studies have investigated the impact of extreme weather events on wind energy variability in specific regions by comparing wind power generation during normal and abnormal weather conditions using observed or simulated wind energy production data. In Western Europe, Leahy et al. found that the wind generation output was low during a prolonged spell of unusually cold conditions in Ireland [18]. Correia et al. evaluated the impact of large-scale atmospheric circulation patterns on monthly wind power resources and production in Portugal [19]. Garrido-Perez et al. assessed the change of wind capacity factors in the United Kingdom and Spain on eight distinct recurring large-scale weather patterns [20]. In China, Li et al. analyzed the characteristics of aggregated wind power generation based on eight typical weather systems in the western region of Inner Mongolia [21]. In addition, scholars have developed many short-term wind power simulation models using physical, statistical learning and hybrid approaches [22–24]. These models provide useful tools to explore the wind power output in abnormal weather conditions for a single wind farm.

However, previous studies have focused on specific sites or relatively small regions, and research to date has not yet investigated the influence of extreme weather events on wind energy production at the interprovincial scale in China. Note that when applying a wind power simulation model to a large number of farms in a wide area, the orientation of each wind farm needs to be considered. This aspect has been somewhat neglected in the model design, as most studies concentrate on the micro-siting layout problem [25]. This study aims to investigate the daily variation and regional differences in wind power output during HW and CW days in six regions in China. We calculate the local prevailing wind direction to determine the orientation of wind farms. Moreover, we explore the monthly changes of HW and CW days in the next several decades under a medium pathway of future greenhouse gas emissions and discuss their potential impact on wind power generation in different regions. It is worth noting that offshore wind farms are also important in China's power system, but their geographical distribution and related extreme weather conditions are completely different from onshore wind farms. Therefore, this study is intended primarily for the onshore wind energy. A description of the study area, wind power simulation model, the definition of regional HW and CW events, and statistical climate projection methods are given in Section 2. Changes in wind power out during HW and CW days, as well as the future projection of HW and CW frequencies, are presented in Section 3. The main conclusions are summarized in Section 4.

2. Materials and Methods

2.1. Study Area and Historical Climate Data. This study classifies China's provinces into six contiguous regions based on their climate classification and interprovincial power network [26]. The spatial distribution of these regions is illustrated in Figure 1, and Table 1 provides a list of the provinces belonging to each region. Northeast China, consisting of four provinces, is mainly located in the mid-temperate and humid or semihumid climate zones. North China spans six provinces and ranges from the warm temperate and semihumid climate zone to the midtemperate and arid climate zone. Northwest China, comprising five provinces, is mainly located in the midtemperate and arid climate zone. East and Central China encompass four and six provinces, respectively, and they extend across the north to midsubtropical and humid climate zones. South China spans six provinces and ranges from the south subtropical and humid climate zone to the tropical and humid climate zone.

As of May 24, 2022, according to the statistics from Global Energy Monitor (GEM), there are 4184 onshore wind farms in China, and their locations are depicted in Figure 1. Notably, Tibet's installed wind power capacity is only 10 MW, accounting for 0.25% of the province's total volume, and its geospatial information is not recorded by GEM. Thus, Tibet is not considered in our further analysis. To explore the influence of HW and CW events on regional wind energy production, we extract historical hourly climate data (surface maximum and minimum temperature, wind speed, and wind direction) from the ERA5 reanalysis [27] for the past ten years (2012–2021).

2.2. Regional Wind Energy Simulation. To obtain the regional wind power output curve (WPOC) for a given day, we use a methodology that utilizes wind speed and direction data to calculate the wind power generation normalized by the total installed capacity for each wind farm. This calculation is performed using a single wind farm analytical model from Kunakote et al. [28]. The model applies Jensen's wake model to estimate the decay of wind speed after passing through a rotating turbine. The initial wake area is assumed to have the same diameter as the turbine and expands linearly to influence downstream turbines, as illustrated in Figure 2. Based on the conservation of momentum, the velocity in the wake cone can be computed as follows:

$$1 - \frac{V(x)}{V_0} = (1 - \sqrt{1 - C_T}) \left(\frac{D^2}{D(x)^2} \right), \quad (1)$$

$$D(x) = D_0 + 2kx,$$

where D represents the turbine rotor diameter, $D(x)$ is the diameter of the wake disk at a distance of x behind the turbine, V_0 is the initial wind velocity, $V(x)$ is the wind velocity at distance x , C_T is the turbine thrust coefficient, and k is a constant that relies on the hub height and terrain roughness. Additionally, the distance between the centres of the wake cone and the swept area of the downstream turbine

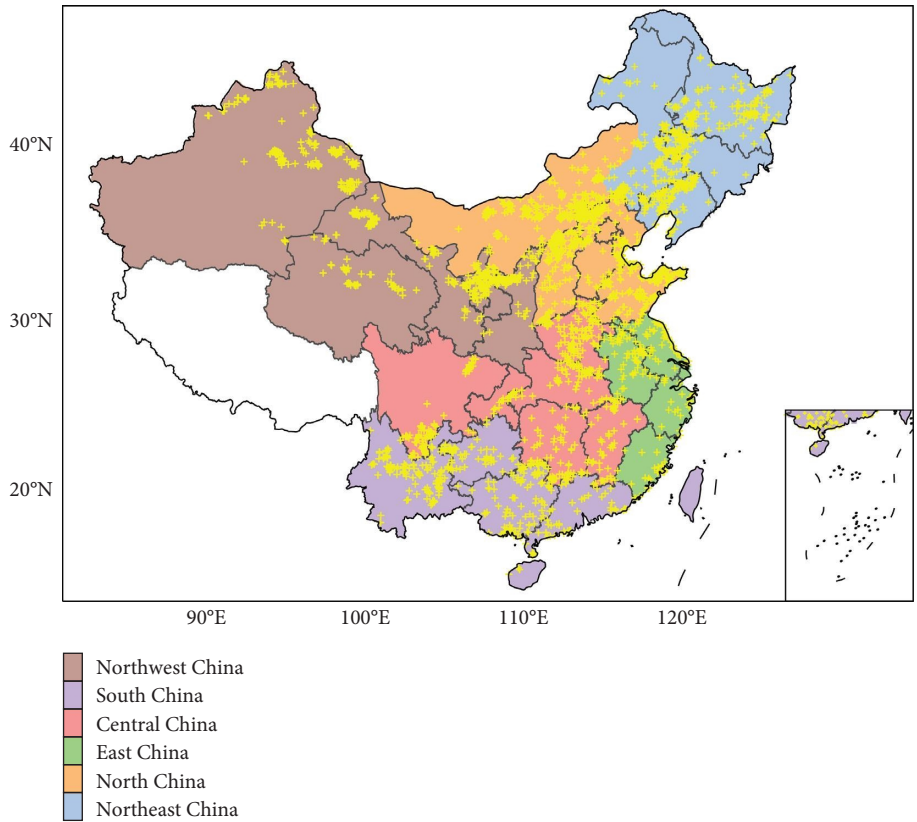


FIGURE 1: Map of the six regions and locations of wind farms (indicated by yellow plus markers) in China.

TABLE 1: Provinces included in the six regions.

Region	Provinces included
Northeast China	Heilongjiang, Liaoning, Jilin, and eastern part of Inner Mongolia
North China	Beijing, Tianjin, Hebei, Shanxi, Shandong, and middle and western parts of Inner Mongolia
East China	Jiangsu, Anhui, Zhejiang, and Fujian
Central China	Henan, Hubei, Hunan, Jiangxi, Chongqing, and Sichuan
South China	Yunnan, Guizhou, Guangxi, Guangdong, Hainan, and Taiwan
Northwest China	Xinjiang, Qinghai, Ningxia, Gansu, and Shaanxi

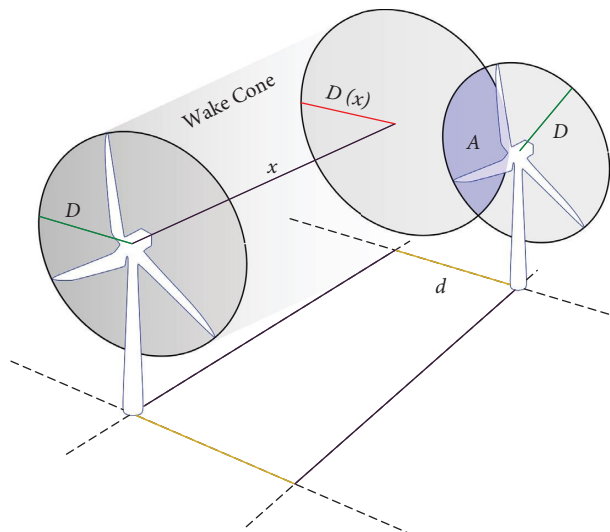


FIGURE 2: Wind turbine wake decay model and its influence on the downstream turbine.

is denoted as d ; therefore, their intersection area (A) can be computed using the following equation:

$$A = D(x)^2 \cos^{-1}\left(\frac{d^2 + D(x)^2 - D^2}{2dD(x)}\right) + D^2 \cos^{-1}\left(\frac{d^2 + D^2 - D(x)^2}{2dD}\right) - \frac{1}{2} \sqrt{(-d + D(x) + D)(d - D(x) + D)(-d + D(x) - D)(d + D(x) + D)}. \quad (2)$$

Real wind industry statistical data and certain assumptions are utilized to determine the layout of wind turbines in each farm. Firstly, referring to the onshore wind power installation list from GEM, it is observed that most existing farms in China were built since the 2010s, with over 65% of them having a capacity of 50 MW (Figure 3). Considering the typical lifespan of a wind farm ranging from 25 to 40 years [29, 30], a capacity of 50 MW will remain the predominant size for Chinese wind farms until 2060. Therefore, for this study, the capacity of individual wind farms is set at 50 MW. Secondly, the primary type of newly installed wind turbines in China is 2 MW [31], corresponding to a mean rotor diameter of 90 m [32], which suggests that each wind farm comprises 25 turbines. Following the design principles of general wind farms [33], these 25 turbines are arranged in a 5-by-5 crossed layout pattern (Figure 4). In this pattern, the orientation of the wind farm (the alignment of turbine rows) is perpendicular to the local prevailing wind direction, and the distance between the rows and columns is set at $7D$ and $4.5D$, respectively. As mentioned earlier, Kunakote's model is employed for a single wind farm, and when applying it to multiple farms in a large region, the orientation of each wind farm needs to be determined. To accomplish this, we divide the compass into 36 directions at 10° intervals and calculate the most frequent wind direction for each wind farm. This calculation is based on hourly eastward and northward wind data at a height of 100 m from ERA5 spanning the period 2012–2021.

After positioning individual wind farms at optimal orientations and simulating their power outputs, we calculate the regional WPOC by averaging the curves from all farms shown in Figure 1 within that region. Since the wind power generation from different farms does not follow an idealized Gaussian distribution, and the arithmetic mean may not be unbiased, we use the biweight robust method [34] to estimate the mean WPOC and mitigate the impact of outliers. The biweight mean y^* for time t is iteratively computed as follows:

$$y^* = \frac{\sum w_i y_i}{\sum w_i}, \quad (3)$$

where y_i represents the wind energy output of the farm i and w_i is a symmetric weight function defined as follows:

$$w_i = \begin{cases} \left(1 - \left(\frac{y_i - y^*}{cS}\right)^2\right)^2, & \text{when } \left(\frac{y_i - y^*}{cS}\right)^2 < 1, \\ 0, & \text{otherwise,} \end{cases} \quad (4)$$

where c is a constant typically ranging from 6 to 9 (set to 7.5 in this study) and S is a robust measure of the standard deviation of the frequency distribution, computed as the median absolute deviation as follows:

$$S = \text{median}\{|y_i - y^*|\}. \quad (5)$$

To initiate the iteration process and compute the final y^* , the median is used as an initial estimate. Due to the non-monotonicity behaviour of the biweight function w_i , the iteration based on equations (3)–(5) may not converge to a constant. However, typically, only three to four iterations are needed to achieve an estimation that changes by no more than 10^{-3} [35]. In this study, the maximum number of iterations is set to 10. Finally, we use a linear-scaling approach [36] to adjust the biases in the mean of capacity factors between observations and simulations. The observed capacity factors are extracted from the China Electric Power Yearbook [37]. It is important to note that we assume the wind farm density remains unchanged as shown in Figure 1, even with an increasing number of wind farms over years, to ensure the applicability of the regional WPOC in the future.

To evaluate the performance of our wind farm model under different weather conditions at local and regional levels, we compare our model simulation with observed power outputs from recent publications [38, 39] for real wind farms in China. For a single wind farm with weather and power output data from 2019–2020 provided by Chen and Xu [38], the correlation coefficients between simulations and observations for hourly mean power output on HW days, CW days, and normal days are 0.988, 0.880, and 0.884, respectively. All correlation coefficients are significant at the 0.001 level, indicating that our model is capable of accurately simulating local wind power under extreme weather conditions. For multiple wind farms within a province, Wan et al. [39] presented the output distribution of several main wind farms in Hubei for three extremely hot days during summer 2016. We also simulate the wind power outputs for the corresponding farms and days to calculate their frequency distribution. The comparison between

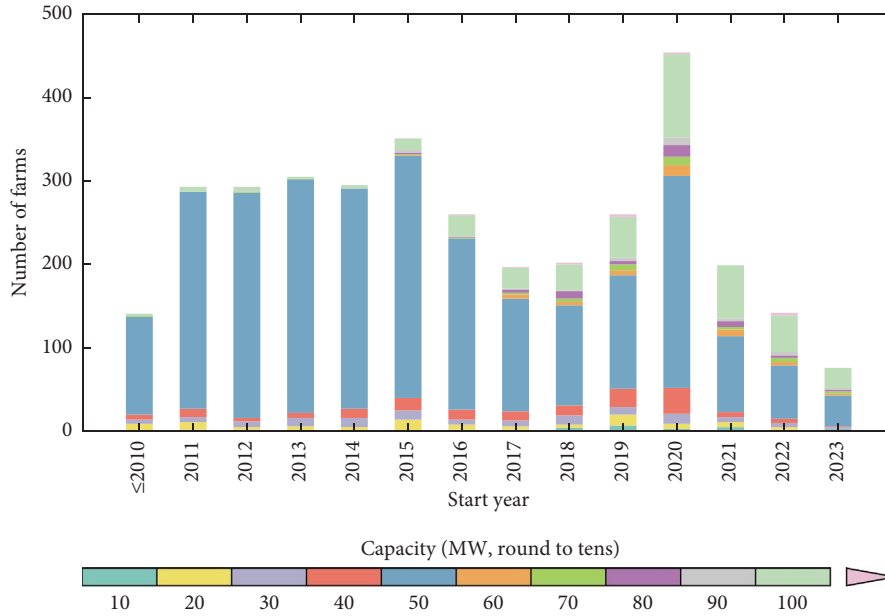


FIGURE 3: Construction of onshore wind farm in China.

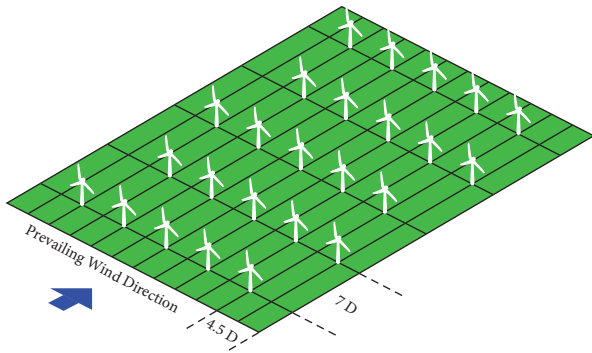


FIGURE 4: Layout of 25 turbines in a wind farm and the prevailing wind direction.

observations and our simulations reveals a similar distribution pattern on hot days (Figure 5). Specifically, the wind power output is below 0.1 for nearly 60% of the time, between 0.1 and 0.2 for approximately 15% of the time, and the output falls into other intervals for less than 10% of the time. The comparison demonstrates the effectiveness of our model at the regional level.

2.3. Identification of Regional Heat Wave and Cold Wave Events. HW and CW events are commonly defined using various criteria, and there is no universally accepted definition for these terms [40]. For a specific location, a basic absolute standard for a hot day is when the daily maximum temperature exceeds 35°C , as proposed by the China Meteorological Administration (CMA). An HW occurs when this hot day condition persists for at least three consecutive days. However, this fixed threshold corresponds to different temperature percentiles across a large region, and it is more reasonable to define a hot day based on a relative threshold

that represents regional heat conditions [41–43]. In this study, we adopt the definition used in previous research [41] and define a hot day at the regional level as one where the daily maximum temperature, averaged over the entire region, exceeds the 98th percentile. Similarly, a regional HW is defined as a hot day condition that lasts for three or more consecutive days.

The criterion for identifying a CW at a specific weather station is when the daily minimum temperature is lower than 4°C and decreases by at least $8/10/12^{\circ}\text{C}$ within the previous 24/48/72-hour period, as established by the CMA. For the regional CW, previous studies suggest that it occurs when the number of sites in a region that meet the station-level criterion exceeds a predefined percentage threshold, such as 20% or 30% for midlatitudes [44, 45]. However, the percentage threshold may be lower (e.g., 10%) for regions in tropical provinces [46]. In this study, we set the percentage threshold as 10% in South China and 20% in other regions. Furthermore, we exclude CW days with a daily minimum temperature below -20°C from the wind power generation analysis since wind turbines may shut down due to extremely low temperatures, resulting in unreliable operation.

2.4. Machine Learning to Optimize Projection of Regional Heat and Cold Waves. To estimate the monthly changes in HW and CW days for six regions in the future, we utilize multiple model results from the Coupled Model Intercomparison Project Phase 6 (CMIP6). CMIP6 offers various standard scenarios that represent different socioeconomic environments and the intensity of the additional radiative forcing in the future [47]. Among these scenarios, the SSP245 scenario closely aligns with the real-world warming projections, taking into account current and long-term actions or policies such as China’s carbon dioxide peaking and carbon neutrality targets [48]. Therefore, we project the potential

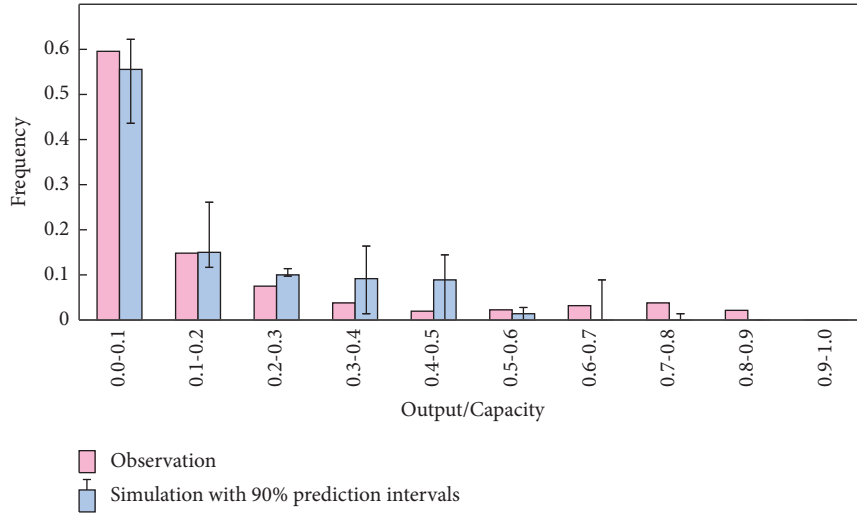


FIGURE 5: Distribution of wind power output from observations and simulations for wind farms in Hubei during three extremely hot days in summer 2016.

changes in HW and CW days during the periods of 2031–2040, 2041–2050, and 2051–2060 based on the SSP245 scenario.

CMIP6 encompasses more than 30 general circulation models (GCMs) and five of them (ACCESS-CM2, FGOALS-g3, IPSL-CM6A-LR, MPI-ESM-2-0, and NESM3) are selected to use for this study. These models have demonstrated superior performance in simulating temperature change trends compared to observed records during the historical period of 1979–2014 [49]. Detailed information on the selected models is provided in Table 2. The model simulation data is obtained from the NASA Earth Exchange Global Daily Downscaled Projections (NEX-GDDP-CMIP6) [50], which applies bias correction and spatial disaggregation procedures to the original CMIP6 output. The processed datasets from NEX-GDDP-CMIP6 maintain a spatial resolution of $0.25^\circ \times 0.25^\circ$ and exhibit better consistency with historical climate records.

The most commonly used approach to project future changes in climate variables from multiple models is to calculate their arithmetic mean. However, recent studies have highlighted the significant advancements of the stacking ensemble method in the machine learning framework. This method involves using the prediction results of the previous level learners as input for the next level [51, 52]. Therefore, in this study, we use the stacking ensemble machine learning method to project changes in HW and CW days under the SSP245 scenario. The model structure is illustrated in Figure 6 and implemented using the ensemble learning toolbox (ELT, available at <https://github.com/vhrique/ELT>). To calibrate the stacking ensemble model, we utilize historical simulations of daily maximum and minimum temperature from the five selected CMIP6 models, along with ERA5 data as observational reference, covering the period from 1990 to 2014. The dataset is divided into a training set and a testing set in a 2:1 ratio, with every

3rd value in the time dimension selected [53]. The base learner for the stacking ensemble is the random forest model initialized by support vector regression, and the hyper-parameters are predefined using the inbuilt configurations from ELT. In order to assess the model performance, we calculate three metrics: the correlation coefficient (r), root-mean-squared error (RMSE), and mean absolute error (MAE), as recommended by prior studies [52, 53].

3. Results and Discussion

3.1. Prevailing Wind Direction in China. Figure 7 shows the prevailing wind direction at a height of 100 m in China with a spatial resolution of 0.25° based on hourly ERA5 reanalysis data over a 10-year period (2012–2021). The wind patterns exhibit a distinct association with the topography of the region. The Northeast China Plain and the North China Plain experience predominantly southwest winds, while the middle and lower reaches of the Yangtze River are characterized by east and southeast winds. The Inner Mongolia Plateau and the hilly and mountainous regions of South China are marked by north and northwest winds. The Sichuan Basin and the Tarim Basin frequently encounter east winds. The Tibet Plateau and the Yunnan-Guizhou Plateau exhibit strong south and southwest winds. These wind regime characteristics are considered in determining the optimal orientations of wind farms in different locations, and wind energy simulations are conducted for each farm under diverse weather conditions.

3.2. Changes of Wind Power Output on HW Days for Different Regions. According to our defined criteria, regional HW occurred for 47, 41, 54, 48, 36, and 47 days in Northeast China, North China, East China, Central China, South China, and Northwest China, respectively, during the past

TABLE 2: List of CMIP6 general circulation models (GCMs) used in this study.

#	Model name	Institution	Country
1	ACCESS-CM2	Commonwealth Scientific and Industrial Research Organisation/Australian Research Council Centre of Excellence for Climate System Science	Australia
2	FGOALS-g3	Chinese Academy of Sciences	China
3	IPSL-CM6A-LR	Institut Pierre Simon Laplace	France
4	MRI-ESM2-0	Meteorological Research Institute	Japan
5	NESM3	Nanjing University of Information Science and Technology	China

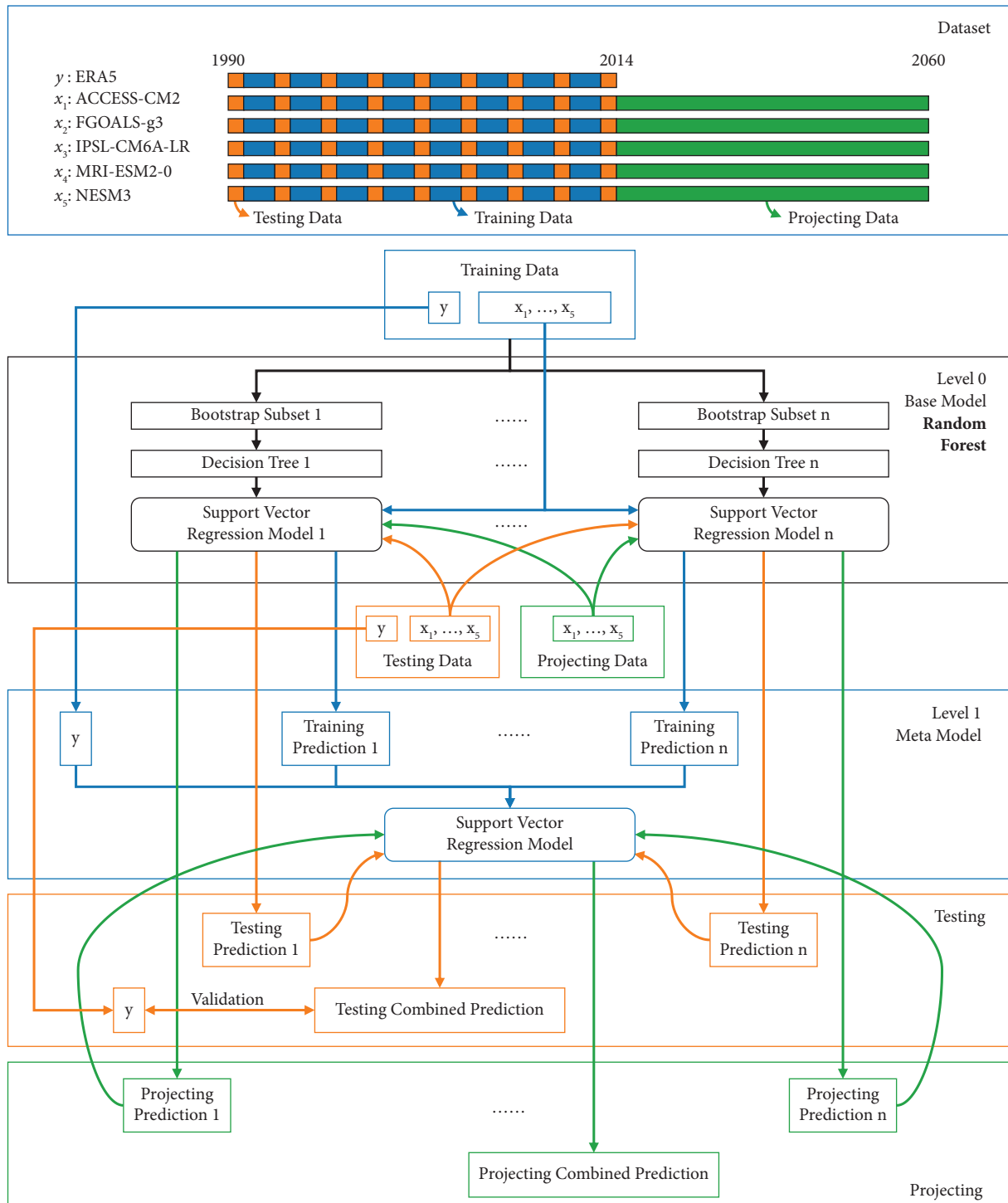


FIGURE 6: Structure of the stacking ensemble learning model for projecting regional HW and CW.

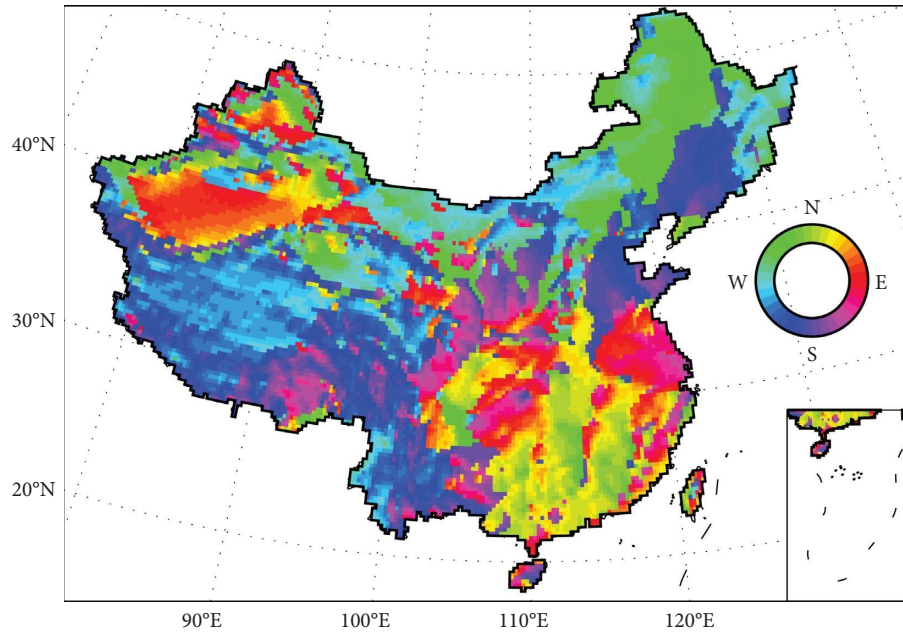


FIGURE 7: Prevailing wind direction at a height of 100 m in China based on hourly ERA5 reanalysis data.

10 years. We conducted simulations to estimate the WPOC for each HW day and normal day (days that were neither a hot day nor a CW day) in summer season (June to August). Subsequently, we calculated the biweight robust mean WPOCs for the six regions under these two weather conditions. The results are presented in Figure 8.

In Northeast China (Figure 8(a)), the WPOC on a summer normal day exhibits two peaks and two valleys. The highest peak output occurs at midnight, reaching 16.6%, while the other peak at 3 PM has an output power of 14.5%. The output drops to 12.1% and 13.0% at 8 AM and 6 PM, respectively. In contrast, the WPOC for an HW day shows a significant reduction of 2–5% from early morning to the afternoon, with an increase of 2–4% in the evening. The wind power production on an HW day is 94.6% of that on a summer normal day.

In North China (Figure 8(b)), the WPOC on a summer normal day is similar to that in Northeast China, but the output in the first valley around 8 AM is slightly lower at 10.2%, and the time of the afternoon peak appears a little later at 5 PM. On the other hand, the WPOC for an HW day has a decline of 3–4% during the day (8 AM to 5 PM) and rises about 2% during the night (9 PM to 5 AM). The wind power production on an HW day is 96.1% of that on a summer normal day.

In East China (Figure 8(c)), the WPOC on a summer normal day also follows a two-peak and two-valley pattern, but the range of wind power output is larger than that in Northeast China and North China. The highest peak output occurs at 10 PM, reaching 19.9%. The other peak is around 5 PM with an output power of 17.7%. Two output valleys are observed at 8 AM and 6 PM, with outputs of 14.5% and 16.2%, respectively. By comparison, the WPOC for an HW day drops about 2% during the day (8 AM to 5 PM) but grows by 2% during the night (9 PM to 5 AM). The wind

power production on an HW day is 99.3% of that on a summer normal day.

In Central China (Figure 8(d)), the WPOC on a summer normal day is similar to that in North China, but the daily output is slightly lower (about 1%), and the peak at night occurs a little earlier at 10 PM. By contrast, the WPOC for an HW day shows a remarkable increase of 2% at night (7 PM to 2 AM), a slight reduction in the morning (7 AM to 12 PM), and no significant changes in the afternoon (2 PM to 6 PM). The wind power production on an HW day is 101.7% of that on a summer normal day.

In South China (Figure 8(e)), the WPOC on a summer normal day still exhibits a two-peak and two-valley pattern, with the highest peak of 21.0% occurring in the afternoon at 3 PM, which is 2% higher than the other peak at 9 PM. Additionally, the output falls to low points of 17.5% and 18.2% at 6 AM and 6 PM, respectively. By comparison, the WPOC for an HW day maintains almost the same output during the nighttime period (8 PM to 5 AM) but experiences a sharp decrease of 3–5% during the daytime period (6 AM to 5 PM). Consequently, the afternoon peak on an HW day is slightly lower than the evening peak. The wind power production on an HW day is 93.2% of that on a summer normal day.

In Northwest China (Figure 8(f)), both summer normal days and HW days show a simple one-peak and one-valley pattern, where the valley occurs at 9 AM and the peak appears before midnight. Both WPOCs have comparable output from 9 AM to 6 PM, while the output on HW days can reach 25.4% at night, which is 5% higher than that on summer normal days. Therefore, the wind power production on an HW day is 109.2% of that on a summer normal day.

Taken together, most regions experience a reduction in wind power output from late morning to early afternoon on HW days. However, this period corresponds to the peak load

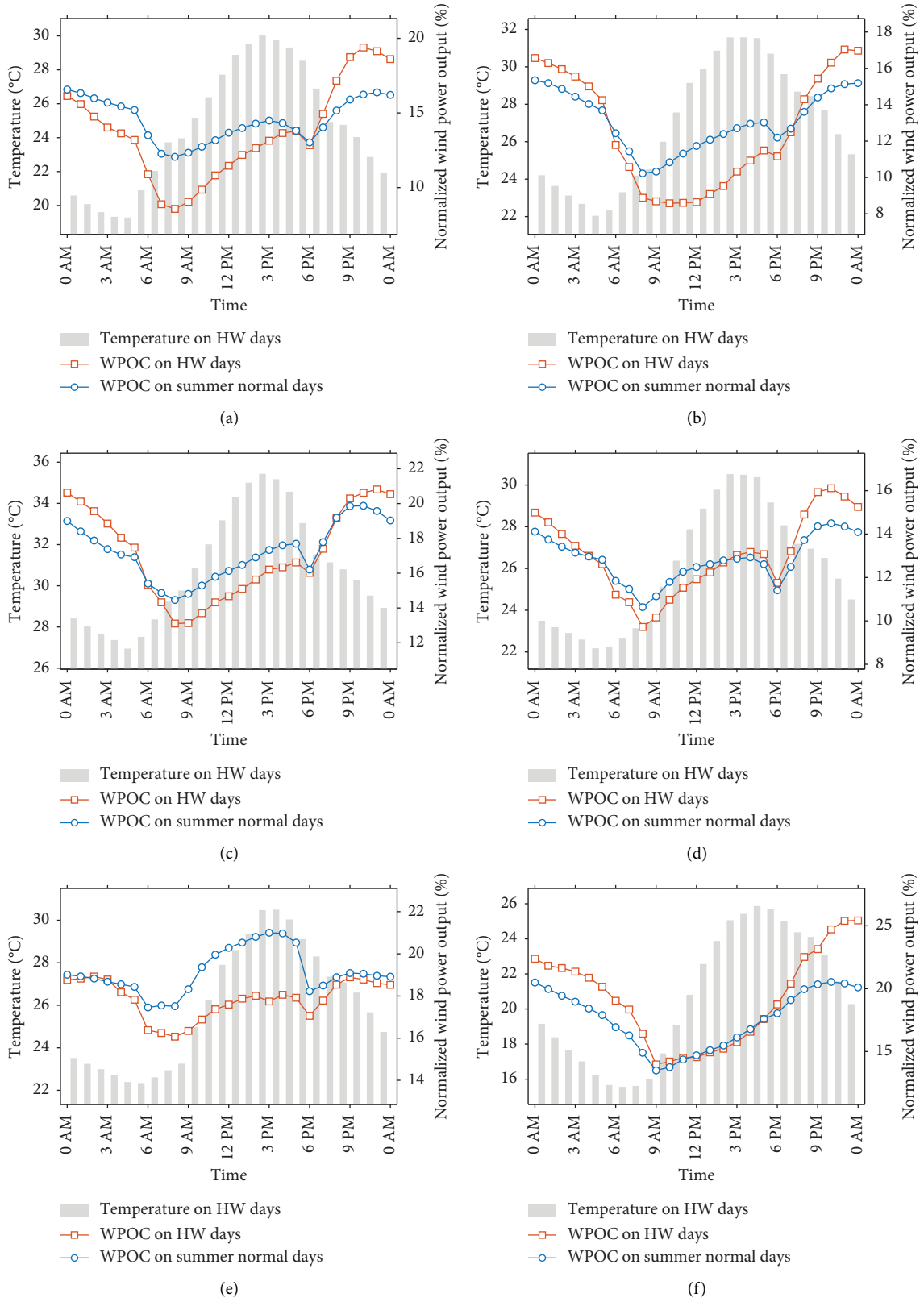


FIGURE 8: Comparison of the ensemble mean WPOCs on HW days and normal days for six regions in China. (a) Northeast China. (b) North China. (c) East China. (d) Central China. (e) South China. (f) Northwest China.

in the commercial sector and the second-highest power demand peak in residential and industrial sectors for typical daily power load curves in summer [54]. Therefore, HW events challenge the daily dynamic supply-demand balancing capability of a power grid that relies on wind resources.

3.3. Changes of Wind Power Output on CW Days for Different Regions. In the past 10 years, there were 106, 96, 21, 5, 8, and 8 days of regional CW in Northeast China, North China, East China, Central China, South China, and Northwest China, respectively. Figure 9 presents the biweight robust mean WPOCs for CW days and normal days in autumn, winter, and spring (AWS) in the six regions. Since the daily minimum temperature typically occurs from midnight to early morning, we also include the mean WPOC for one day before and after the CW event, and these two days are excluded from the count of normal days.

In Northeast China (Figure 9(a)), the WPOC on an AWS normal day follows the same two-peak and two-valley pattern as a summer normal day. However, the average output is 7.9% higher, with the peak output reaching 24.9% before midnight (11 PM). In contrast, the output from the day before CW until noon on the CW day shows a significant increase of 15–20%, followed by a rapid decline. By the evening of the CW day and throughout the next day, the WPOC is about 3–4% lower than that on an AWS normal day.

In North China (Figure 9(b)), the WPOC on an AWS normal day also exhibits two peaks and two valleys. The highest peak output is 21.1%, which appears in the afternoon (3 PM). The other peak is around midnight with an output power of 20.7%. The output drops to low points of 16.4% and 18.0% at 10 AM and 7 PM, respectively. The WPOCs on the CW day and adjacent days are all higher than that on an AWS normal day. The largest increase (about 10–12%) occurs from the CW day to the afternoon of the next day, while the output on the day before the CW only has a slight growth of 2–6%.

In East China (Figure 9(c)), the WPOC on an AWS normal day follows a simple one-peak and one-valley pattern, with the valley (16.6%) observed at 10 AM and the peak (21.2%) occurring before midnight. By comparison, the output is about 4% lower in the morning of the day before the CW, then sharply increases, reaching a peak of 47.8% at 3 PM on the CW day, and gradually returns to the normal level on the day after the CW.

In Central China (Figure 9(d)), the WPOC on an AWS normal day is similar to that in East China, but the output is lower (about 6%). By contrast, the output remains at the normal level in the early morning of the day before the CW and then gradually increases. It reaches over 60% generation from early morning until 4 PM on the CW day, and then slowly decreases but remains above the normal WPOC on the day after CW.

In South China (Figure 9(e)), the WPOC on an AWS normal day also exhibits a one-peak and one-valley pattern, with the valley (19.5%) observed at 10 AM and the peak

(26.0%) occurring in the afternoon (5 PM). By comparison, the increase in output on the CW day is about 15%, but it can reach 20–25% within the 12-hour period before and after the CW day.

In Northwest China (Figure 9(f)), the WPOC on an AWS normal day also shows a one-peak and one-valley pattern, with the valley (14.2%) observed at 11 AM and the peak (18.2%) occurring in the evening. In contrast, the output starts to increase from the early morning of the day before the CW and reaches a peak of 43.7% in the afternoon of the CW day. It then gradually decreases to the normal level on the day after the CW, with a significant upturn around 2 PM.

In summary, all regions experience higher wind power generation on the CW day and the day before. Residential, commercial, and industrial sectors typically demand less energy during winter, as reflected in typical daily power load curves [54]. Therefore, power supplies face fewer challenges on CW days compared to HW days. However, it is worth noting that on the day after a CW event, there is a significant reduction in wind power output while electricity consumption experiences notable growth, particularly in the residential sector, due to cold weather [55]. This situation may increase the risk of wide-area power outages.

3.4. Future Changes of the HW and CW Days. Table 3 shows the performance of applying stacking ensemble models in the test phase for predicting HW and CW days over 6 regions, respectively. All models obtain skilful performance, with r ranging from 0.792 to 0.976, RMSE ranging from 0.065 days to 0.420 days, and MAE ranging from 0.039 days to 0.290 days. Although models for CW days exhibit superior results than that for HW days, all the correlation coefficients pass the 0.01 significance level, which indicates that they effectively capture the temporal characteristics of HW and CW days among regions and could be used to project future changes.

Figure 10 depicts the change in the number of HW days for each month during the past decade and the next three decades under the SSP245 scenario. The figure reveals a continuous increase in the number of HW days in each region during 2031–2040, 2041–2050, and 2051–2060, with significant regional differences in the number of increasing days. When compared to 2012–2021, the total number of HW days per year will increase by 1.5 to 3.9 times in 2031–2040, 1.4 to 4.2 times in 2041–2050, and 2.5 to 6.5 times in 2051–2060. The minimum increase in HW days is expected in North China, while Central China and South China are expected to have the maximum increase. For instance, Central China and South China will have approximately 10 HW days in July during 2051–2060. Furthermore, the month with the highest number of HW days will gradually shift from August to July in these two regions. Prior studies have mostly focused on the mean summer temperature change in the future and reported that the warming trend in Northeast China is large but small over South China [56–58]. However, a roughly reversed spatial pattern is seen for high temperatures, such as the number of

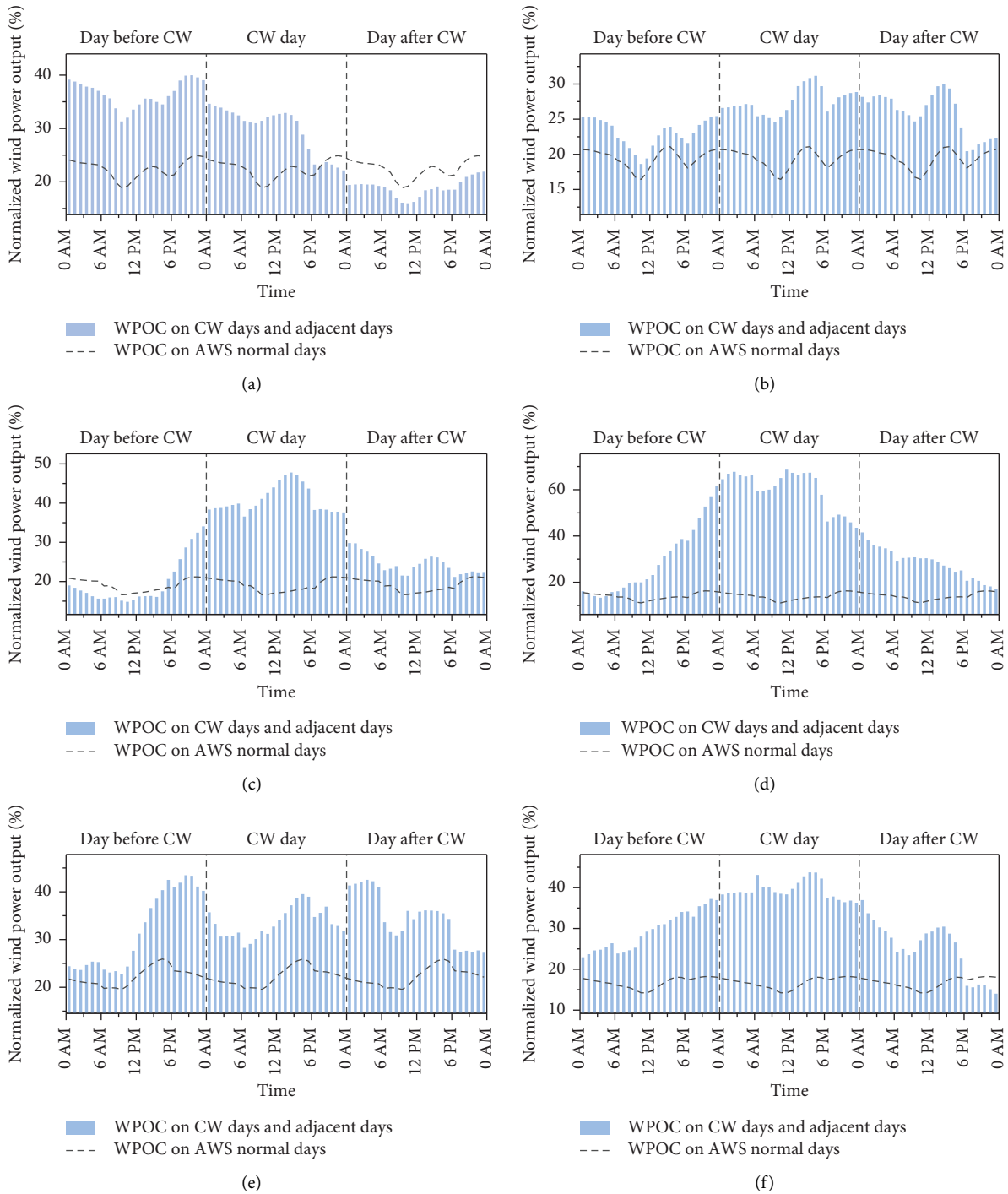


FIGURE 9: Ensemble mean WPOCs on CW days and adjacent days and their comparison with WPOCs on normal days for six regions in China. (a) Northeast China. (b) North China. (c) East China. (d) Central China. (e) South China. (f) Northwest China.

warm days, warm spell duration indicators [59], and HW days in this study. Hence, the increased number of HW days in the future could lead to a higher likelihood of supply-demand imbalance from late morning to early afternoon.

Unlike HW days, the change in CW days is relatively small and does not have coherent trends among regions (Figure 11). Compared with 2012–2021, the change of total CW days over a year ranges from 80% to 183% times

TABLE 3: The stacking ensemble model performance (r , RMSE, and MAE) during the test phase for predicting HW and CW days over six regions in China.

Region	HW			CW		
	r	RMSE	MAE	r	RMSE	MAE
Northeast China	0.806	0.325	0.212	0.900	0.420	0.290
North China	0.926	0.338	0.163	0.940	0.218	0.173
East China	0.892	0.149	0.114	0.976	0.049	0.041
Central China	0.840	0.283	0.164	0.869	0.072	0.039
South China	0.792	0.161	0.091	0.844	0.070	0.042
Northwest China	0.836	0.179	0.145	0.897	0.065	0.047

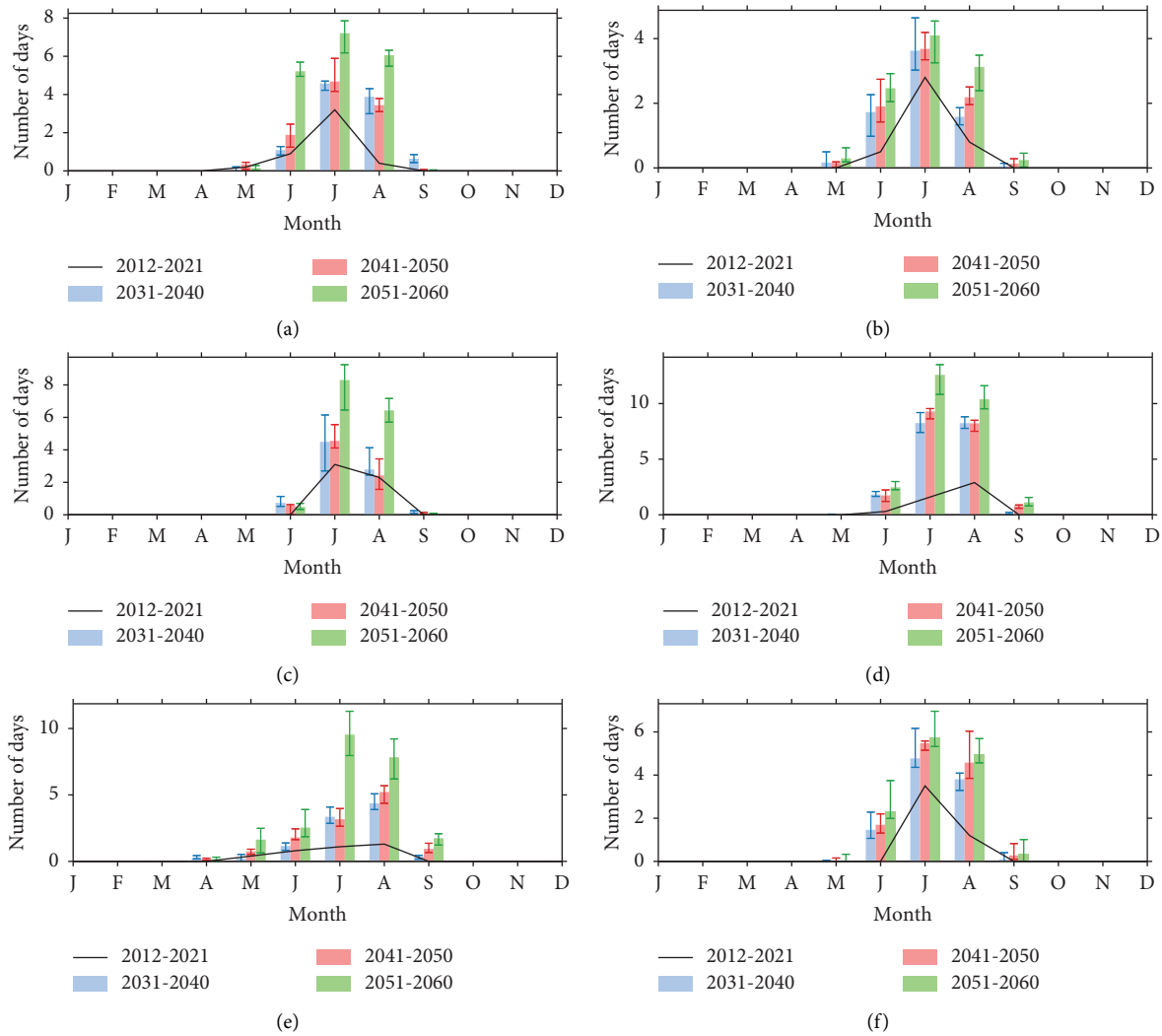


FIGURE 10: Change of HW days in each month for six regions over the past 10 years (2012–2021) and three decades (2031–2040, 2041–2050, and 2051–2060) under the SSP245 scenario. Error bars represent 90% confidence intervals by the bootstrap process. (a) Northeast China. (b) North China. (c) East China. (d) Central China. (e) South China. (f) Northwest China.

in 2031–2040, from 55% to 120% times in 2041–2050, and from 87% to 128% times in 2051-2060. Specifically, the number of annual CW days increases significantly in Central China, decreases slightly in East China and

Northwest China, but remains steady in the other three regions. Moreover, the monthly distribution of CW days changes a lot for most regions, i.e., CW days decline in February and November but grow in December and

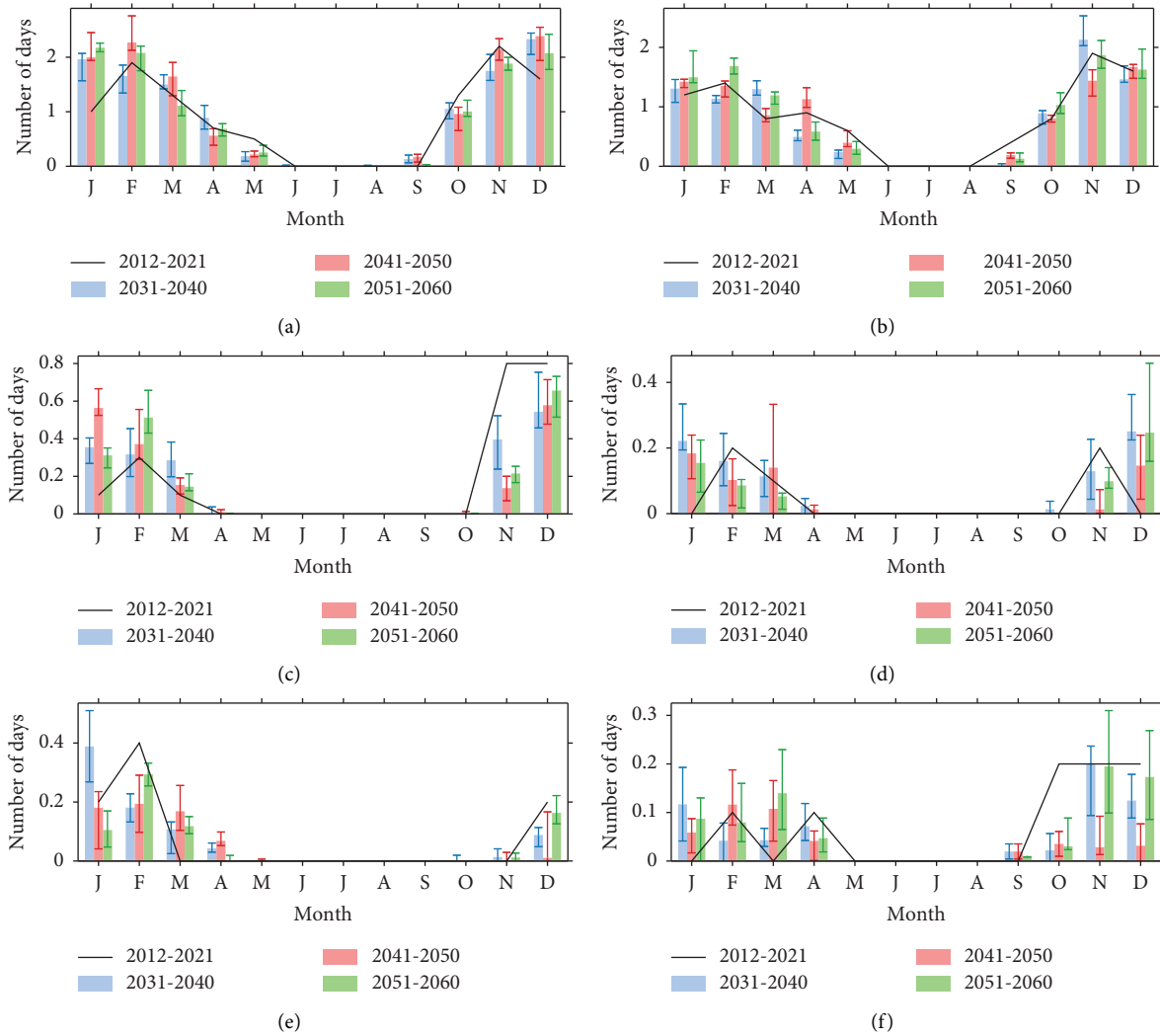


FIGURE 11: Change of CW days in each month for six regions over the past 10 years (2012–2021) and three decades (2031–2040, 2041–2050, and 2051–2060) under the SSP245 scenario. Error bars represent 90% confidence intervals by the bootstrap process. (a) Northeast China. (b) North China. (c) East China. (d) Central China. (e) South China. (f) Northwest China.

January for Central China, CW days decline in November and December but grow from January to March for East China, CW days increase in March for South China, CW days decrease in October and December but increase in January and March for Northwest China, and CW days decrease in March and October but increase in December

and January Northeast China. Previous studies have reported that winter temperature will increase in most regions of China over the 21st century [56–58], but the frequency of cold extremes will not experience a notable decline along with the warming trend [60], including the CW events in this study. Consequently, the impacts of CW

TABLE 4: Relative wind power output anomaly on HW and CW days and the expected change in the number of HW and CW days per year in 2031–2040, 2041–2050, 2051–2060, and 2051–2060.

Region	HW					CW						
	Output for HW (%)	2031–2040 (d/yr)	2041–2050 (d/yr)	2051–2060 (d/yr)	Output for CW (%)	2031–2040 (d/yr)	2041–2050 (d/yr)	2051–2060 (d/yr)	Output for CW (%)	2031–2040 (d/yr)	2041–2050 (d/yr)	2051–2060 (d/yr)
Northeast China	-5.43	+5.5	+5.7	+13.9	+26.51	+1.0	+1.9	+0.8	+26.51	+1.0	+1.9	+0.8
North China	-3.88	+3.1	+4.0	+6.1	+31.14	-0.6	-0.3	+0.3	+31.14	-0.6	-0.3	+0.3
East China	-0.67	+2.8	+2.3	+9.9	+48.96	-0.2	-0.3	-0.3	+48.96	-0.2	-0.3	-0.3
Central China	+1.73	+13.7	+15.3	+21.8	+179.98	+0.4	+0.1	+0.1	+179.98	+0.4	+0.1	+0.1
South China	-6.78	+6.1	+8.5	+19.9	+49.84	0.0	-0.2	-0.1	+49.84	0.0	-0.2	-0.1
Northwest China	+9.22	+5.4	+7.3	+8.7	+87.16	-0.2	-0.4	0.0	+87.16	-0.2	-0.4	0.0

on the power supply in the day after CW still exist and their monthly distribution will experience a notable change in the future.

Table 4 summarizes the relative wind power output anomaly on HW and CW days, as well as the expected change in the number of HW and CW days per year in the future.

4. Conclusions and Discussion

In this study, we calculate the local prevailing wind direction to determine the orientation of wind farms and then simulate the daily wind power output during HW and CW days for six regions in China. The major findings can be drawn as follows. (1) Most regions (except for Northwest China) experience a significant wind power output reduction from late morning to early afternoon on HW days, which challenges the daily dynamic supply-demand balancing capability of a power grid. (2) All regions receive more wind power generation on the CW day and the previous day than on normal days. The output peak occurs in the evening of the previous day for Northeast China and South China, while it appears in the early afternoon for other regions. However, a rapid decline in wind power is seen on the day after the CW for all regions, which may increase the risk of wide-area power outages.

In addition, we apply the stacking ensemble machine learning method to project the changes of regional HW and CW days during 2031–2040, 2041–2050, and 2051–2060 based on the SSP245 scenario. In the future, HW days have coherent growing trends among regions but CW days mainly show monthly redistributions without notable changes in total occurrences throughout the year. Therefore, HW and CW events will mainly influence the intraday and interday supply-demand balances of the power grid that depends on wind resources.

In view of the method, the originality of this study is that it explores wind energy production at the interprovincial scale by placing individual wind farm models into a prevailing wind direction network and applying an ensemble learning algorithm to estimate the extreme weather change in the future from multiple GCMs. This method can better extract complex dynamical processes and implicit wind patterns within climate models and it differs from previous regional wind power simulators mainly based on statistical relationships [7, 61].

A number of limitations need to be noted regarding the present study. Firstly, we only focus on the wind power sector during HW and CW days; further work is required to identify the output of hybrid renewable energy systems under different extreme weather conditions. Secondly, we simply assume that the wind farm density remain unchanged in the future with a growing number of wind farms, which will induce gradually increased bias of regional WPOCs. Further research might develop a dynamic wind farm network based on long-term planning of wind projects to reduce such bias.

Data Availability

The ERA5 reanalysis data used to support the findings of this study have been deposited in the <https://www.ecmwf.int/en/forecasts/datasets/reanalysis-datasets/era5> repository. The wind farm location data used to support the findings of this study have been deposited in the <https://globalenergymonitor.org/repository>. The NEX-GDDP-CMIP6 data used to support the findings of this study have been deposited in the <https://registry.opendata.aws/nex-gddp-cmip6/> repository.

Conflicts of Interest

The authors declare that they have no conflicts of interest regarding the publication of this paper.

Acknowledgments

This work was supported by the Science and Technology Foundation of SGCC (grant no. 5100-202155466A-0-0-00). We acknowledge the World Climate Research Programme, which, through its working group on coupled modelling, coordinated and promoted CMIP6.

References

- [1] J. Wu, Y. Shi, and Y. Xu, "Evaluation and projection of surface wind speed over China based on CMIP6 GCMs," *Journal of Geophysical Research: Atmospheres*, vol. 125, no. 22, 2020.
- [2] Y. Liu, H. Cui, and Q. Ge, "Classification of wind use level and required investment for countries below average to upgrade," *Journal of Cleaner Production*, vol. 211, pp. 1427–1433, 2019.
- [3] K. Eureka, P. Sullivan, M. Gleason, D. Hettlinger, D. Heimiller, and A. Lopez, "An improved global wind resource estimate for integrated assessment models," *Energy Economics*, vol. 64, pp. 552–567, 2017.
- [4] X. Fu and H. Niu, "Key technologies and applications of agricultural energy internet for agricultural planting and fisheries industry," *Information Processing in Agriculture*, Elsevier, Amsterdam, Netherlands, 2022.
- [5] C. M. Grams, R. Beerli, S. Pfenninger, I. Staffell, and H. Wernli, "Balancing Europe's wind-power output through spatial deployment informed by weather regimes," *Nature Climate Change*, vol. 7, no. 8, pp. 557–562, 2017.
- [6] N. Kirchner-Bossi, R. García-Herrera, L. Prieto, and R. M. Trigo, "A long-term perspective of wind power output variability," *International Journal of Climatology*, vol. 35, no. 9, pp. 2635–2646, 2015.
- [7] X. Fu, X. Wu, C. Zhang, S. Fan, and N. Liu, "Planning of distributed renewable energy systems under uncertainty based on statistical machine learning," *Protection and Control of Modern Power Systems*, vol. 7, no. 1, p. 41, 2022.
- [8] K. Van Der Wiel, H. C. Bloomfield, R. W. Lee et al., "The influence of weather regimes on European renewable energy production and demand," *Environmental Research Letters*, vol. 14, no. 9, Article ID 094010, 2019.
- [9] L. M. Miller and D. W. Keith, "Climatic impacts of wind power," *Joule*, vol. 2, no. 12, pp. 2618–2632, 2018.
- [10] D. Millstein, J. Solomon-Culp, M. Wang, P. Ullrich, and C. Collier, "Wind energy variability and links to regional and

- synoptic scale weather,” *Climate Dynamics*, vol. 52, no. 7-8, pp. 4891–4906, 2018.
- [11] X. Fu and Y. Zhou, “Collaborative optimization of PV greenhouses and clean energy systems in rural areas,” *IEEE Transactions on Sustainable Energy*, vol. 14, no. 1, pp. 642–656, 2023.
- [12] L. Liu, Y. Wang, Z. Wang et al., “Potential contributions of wind and solar power to China’s carbon neutrality,” *Resources, Conservation and Recycling*, vol. 180, Article ID 106155, 2022.
- [13] G. Wu and D. Niu, “A study of carbon peaking and carbon neutral pathways in China’s power sector under a 1.5 °C temperature control target,” *Environmental Science and Pollution Research*, vol. 29, no. 56, pp. 85062–85080, 2022.
- [14] T. Hu and Y. Sun, “Projected changes in extreme warm and cold temperatures in China from 1.5 to 5°C global warming,” *International Journal of Climatology*, vol. 40, no. 8, pp. 3942–3953, 2020.
- [15] Y. Yang, C. Jin, and S. Ali, “Projection of heat wave in China under global warming targets of 1.5 °C and 2 °C by the ISIMIP models,” *Atmospheric Research*, vol. 244, Article ID 105057, 2020.
- [16] X. Fu, Q. Guo, and H. Sun, “Statistical machine learning model for stochastic optimal planning of distribution networks considering a dynamic correlation and dimension reduction,” *IEEE Transactions on Smart Grid*, vol. 11, no. 4, pp. 2904–2917, 2020.
- [17] X. Fu, “Statistical machine learning model for capacitor planning considering uncertainties in photovoltaic power,” *Protection and Control of Modern Power Systems*, vol. 7, no. 1, p. 5, 2022.
- [18] P. G. Leahy and A. M. Foley, “Wind generation output during cold weather-driven electricity demand peaks in Ireland,” *Energy*, vol. 39, no. 1, pp. 48–53, 2012.
- [19] J. M. Correia, A. Bastos, M. C. Brito, and R. M. Trigo, “The influence of the main large-scale circulation patterns on wind power production in Portugal,” *Renewable Energy*, vol. 102, pp. 214–223, 2017.
- [20] J. M. Garrido-Perez, C. Ordóñez, D. Barriopedro, R. García-Herrera, and D. Paredes, “Impact of weather regimes on wind power variability in western Europe,” *Applied Energy*, vol. 264, Article ID 114731, 2020.
- [21] P. Li, X. Guan, J. Wu, and H. Zheng, *Analyzing Characteristics of Aggregated Wind Power Generation Based on Weather Regime Classification*, vol. 39, no. 7, pp. 1866–1872, 2015.
- [22] Z. Qian, Y. Pei, H. Zareipour, and N. Chen, “A review and discussion of decomposition-based hybrid models for wind energy forecasting applications,” *Applied Energy*, vol. 235, pp. 939–953, 2019.
- [23] J. Maldonado-Correa, J. C. Solano, and M. Rojas-Moncayo, “Wind power forecasting: a systematic literature review,” *Wind Engineering*, vol. 45, no. 2, pp. 413–426, 2021.
- [24] I. K. Bazionis, P. A. Karafotis, and P. S. Georgilakis, “A review of short-term wind power probabilistic forecasting and a taxonomy focused on input data,” *IET Renewable Power Generation*, vol. 16, no. 1, pp. 77–91, 2021.
- [25] J. Feng and W. Z. Shen, “Co-optimization of the shape, orientation and layout of offshore wind farms,” *Journal of Physics: Conference Series*, vol. 1618, no. 4, Article ID 042023, 2020.
- [26] X. Zhou, J. Yi, R. Song, X. Yang, Y. Li, and H. Tang, “An overview of power transmission systems in China,” *Energy*, vol. 35, no. 11, pp. 4302–4312, 2010.
- [27] H. Hersbach, B. Bell, P. Berrisford et al., “The ERA5 global reanalysis,” *Quarterly Journal of the Royal Meteorological Society*, vol. 146, no. 730, pp. 1999–2049, 2020.
- [28] T. Kunakote, N. Sabangan, S. Kumar et al., “Comparative performance of twelve metaheuristics for wind farm layout optimisation,” *Archives of Computational Methods in Engineering*, vol. 29, no. 1, pp. 717–730, 2021.
- [29] S. C. Pryor and R. J. Barthelmie, “A global assessment of extreme wind speeds for wind energy applications,” *Nature Energy*, vol. 6, no. 3, pp. 268–276, 2021.
- [30] B. P. Hayes, A. Wilson, R. Webster, and S. Z. Djokic, “Comparison of two energy storage options for optimum balancing of wind farm power outputs,” *IET Generation, Transmission & Distribution*, vol. 10, no. 3, pp. 832–839, 2016.
- [31] J. Ma and J. Wang, *Modern Testing and Calculation Methods for Wind Turbines*, Northwestern Polytechnical University Press, Xi’an, China, 2019.
- [32] P. Enevoldsen and G. Xydis, “Examining the trends of 35 years growth of key wind turbine components,” *Energy for Sustainable Development*, vol. 50, pp. 18–26, 2019.
- [33] F. Dong, L. Wang, D. Tian, and J. Li, *Introduction to Renewable Energy*, China Environmental Science Press, Beijing, China, 2013.
- [34] F. Mosteller and J. W. Tukey, *Data Analysis and Regression: A Second Course in Statistics*, Addison-Wesley, Boston, MA, USA, 1977.
- [35] E. R. Cook and L. A. Kairiukstis, *Methods of Dendrochronology: Applications in the Environmental Sciences*, Springer, Dordrecht, Netherlands, 1990.
- [36] C. Teutschbein and J. Seibert, “Bias correction of regional climate model simulations for hydrological climate-change impact studies: review and evaluation of different methods,” *Journal of Hydrology*, vol. 456-457, pp. 12–29, 2012.
- [37] China Electricity Council, *China Electric Power Yearbook 2021*, China Statistics Press, Beijing, China, 2021.
- [38] Y. Chen and J. Xu, “Solar and wind power data from the Chinese state grid renewable energy generation forecasting competition,” *Scientific Data*, vol. 9, no. 1, p. 577, 2022.
- [39] L. Wan, K. Zhou, and T. Wang, “Wind power and photovoltaics output characteristic analysis during typical peak load in Hubei grid,” *Hubei Electric Power*, vol. 40, no. 12, pp. 14–18, 2016.
- [40] T. Ding, W. Qian, and Z. Yan, “Changes in hot days and heat waves in China during 1961-2007,” *International Journal of Climatology*, vol. 30, no. 10, pp. 1452–1462, 2010.
- [41] Z. Xu, G. Fitzgerald, Y. Guo, B. Jalaludin, and S. Tong, “Impact of heatwave on mortality under different heatwave definitions: a systematic review and meta-analysis,” *Environment International*, vol. 89-90, pp. 193–203, 2016.
- [42] Q. You, Z. Jiang, L. Kong et al., “A comparison of heat wave climatologies and trends in China based on multiple definitions,” *Climate Dynamics*, vol. 48, no. 11-12, pp. 3975–3989, 2016.
- [43] J. Yang, P. Yin, J. Sun et al., “Heatwave and mortality in 31 major Chinese cities: definition, vulnerability and implications,” *Science of the Total Environment*, vol. 649, pp. 695–702, 2019.
- [44] H. Li, S. Lin, Y. Wang, P. Huang, and Y. Yu, “Characteristics of cold wave activities in Beijing-Tianjin-Hebei region from 1961 to 2017,” *Journal of Arid Meteorology*, vol. 40, no. 1, pp. 41–48, 2022.
- [45] N. Ma, L. He, S. Liang, and J. Guo, “Low-frequency characteristics of winter-time cold air activity in the Beijing-Tianjin-Hebei region and the impacts of low-frequency

- variation of the Siberian High,” *Acta Geographica Sinica*, vol. 75, no. 3, pp. 485–496, 2020.
- [46] W. Liu, S. Y. Huang, D. Li, C. Wang, X. Zhou, and S. Chen, “Spatiotemporal computing of cold wave characteristic in recent 52 years: a case study in Guangdong Province, South China,” *Natural Hazards*, vol. 79, no. 2, pp. 1257–1274, 2015.
- [47] B. C. O’neill, E. Kriegler, K. L. Ebi et al., “The roads ahead: narratives for shared socioeconomic pathways describing world futures in the 21st century,” *Global Environmental Change*, vol. 42, pp. 169–180, 2017.
- [48] S. Boehm, L. Jeffery, and K. Levin, “State of climate action 2022, climate action tracker, climate analytics,” *The United Nations Climate Change High-Level Champions*, World Resources Institute, Washington, DC, USA, 2022.
- [49] Q. You, Z. Cai, F. Wu, Z. Jiang, N. Pepin, and S. S. P. Shen, “Temperature dataset of CMIP6 models over China: evaluation, trend and uncertainty,” *Climate Dynamics*, vol. 57, no. 1-2, pp. 17–35, 2021.
- [50] B. Thrasher, W. Wang, A. Michaelis, F. Melton, T. Lee, and R. Nemani, “NASA global daily downscaled projections, CMIP6,” *Scientific Data*, vol. 9, no. 1, p. 262, 2022.
- [51] B. Pavlyshenko, “Using Stacking Approaches for Machine Learning Models,” in *Proceedings of the 2018 IEEE Second International Conference on Data Stream Mining & Processing (DSMP)*, pp. 255–258, Lviv, Ukraine, August 2018.
- [52] Z. Jiang, S. Yang, Z. Liu et al., “Can ensemble machine learning be used to predict the groundwater level dynamics of farmland under future climate: a 10-year study on Huaibei Plain,” *Environmental Science and Pollution Research*, vol. 29, no. 29, pp. 44653–44667, 2022.
- [53] A. Livera, M. Theristis, and G. Makrides, “Optimal development of location and technology independent machine learning photovoltaic performance predictive models,” in *Proceedings of the 2019 IEEE 46th Photovoltaic Specialists Conference (PVSC)*, pp. 1270–1275, Chicago, IL, USA, June 2019.
- [54] W. Sheng, K. Liu, H. Pei, Y. Li, D. Jia, and Y. Diao, “A fast reactive power optimization in distribution network based on large random matrix theory and data analysis,” *Applied Sciences*, vol. 6, no. 6, p. 158, 2016.
- [55] Z. Y. Zhang, D. Y. Gong, and J. J. Ma, “A study on the electric power load of Beijing and its relationships with meteorological factors during summer and winter,” *Meteorological Applications*, vol. 21, no. 2, pp. 141–148, 2014.
- [56] K. Lu, M. Arshad, X. Ma, I. Ullah, J. Wang, and W. Shao, “Evaluating observed and future spatiotemporal changes in precipitation and temperature across China based on CMIP6-GCMs,” *International Journal of Climatology*, vol. 42, no. 15, pp. 7703–7729, 2022.
- [57] H. Zhu, Z. Jiang, and L. Li, “Projection of climate extremes in China, an incremental exercise from CMIP5 to CMIP6,” *Science Bulletin*, vol. 66, no. 24, pp. 2528–2537, 2021.
- [58] X. Yang, B. Zhou, Y. Xu, and Z. Han, “CMIP6 evaluation and projection of temperature and precipitation over China,” *Advances in Atmospheric Sciences*, vol. 38, no. 5, pp. 817–830, 2021.
- [59] G. Zhang, G. Zeng, X. Yang, and Z. Jiang, “Future changes in extreme high temperature over China at 1.5°C–5°C global warming based on CMIP6 simulations,” *Advances in Atmospheric Sciences*, vol. 38, no. 2, pp. 253–267, 2021.
- [60] L. Wei, L. Liu, C. Jing et al., “Simulation and projection of climate extremes in China by a set of statistical downscaled data,” *International Journal of Environmental Research and Public Health*, vol. 19, no. 11, p. 6398, 2022.
- [61] Z. Wang, W. Wang, C. Liu, Z. Wang, and Y. Hou, “Probabilistic forecast for multiple wind farms based on regular vine copulas,” *IEEE Transactions on Power Systems*, vol. 33, no. 1, pp. 578–589, 2018.